Communication

# Template-Free Synthesis of Periodic Three-Dimensional PbSe Nanostructures via Photoelectrodeposition

Azhar I. Carim, Kathryn R Hamann, Nicolas A Batara, Jonathan R Thompson, Harry A Atwater, and Nathan S. Lewis

*J. Am. Chem. Soc.*, **Just Accepted Manuscript** • DOI: 10.1021/jacs.8b02931 • Publication Date (Web): 09 May 2018

# Template-Free Synthesis of Periodic Three-Dimensional PbSe Nanostructures via Photoelectrodeposition

Azhar I. Carim[†,⊥], Kathryn R. Hamann[†,⊥], Nicolas A. Batara[‡], Jonathan R. Thompson[‡], Harry A. Atwater[‡] and Nathan S. Lewis[†,§,ǁ,*]

[†]Division of Chemistry and Chemical Engineering, [‡]Division of Engineering and Applied Sciences, [§]Kavli Nanoscience Institute, [ǁ]Beckman Institute, California Institute of Technology, Pasadena, California 91125, United States.

*Supporting Information Placeholder*

**ABSTRACT:** Highly periodic, geometrically directed, anisotropic Se-Pb films have been synthesized at room temperature from an isotropic aqueous solution without the use of physical templates, by photoelectrodeposition using a series of discrete input illumination polarizations and wavelengths from an unstructured, uncorrelated, incoherent light source. Dark growth did not generate deposits with substantial long-range order, but growth using unpolarized illumination resulted in an ordered, nanoscale, mesh-type morphology. Linearly polarized illumination generated Se-Pb deposits that displayed an ordered, highly anisotropic lamellar pattern wherein the long axes of the lamellae were aligned parallel to the light polarization vector. The pitch of the lamellar features was proportional to the input light wavelength, as confirmed by Fourier analysis. Full-wave electromagnetic and Monte Carlo growth simulations that incorporated only the fundamental light-matter interactions during growth successfully reproduced the experimentally observed morphologies and quantitatively matched the pattern periodicities. Electrochemical post-processing of the as-deposited Se-Pb structures resulted in the generation of stoichiometric, crystalline PbSe while preserving the nanopatterned morphology, thus broadening the genus of materials that can be prepared with controlled three-dimensional morphologies through maskless photoelectrodeposition.

Arrays of semiconductor mesostructures have been extensively developed for electronic, photonic and sensing applications, due to unique physical properties realized by patterning at the micro- and nanoscale.[1-3] Conventional photolithographic patterning involves selective exposure of a chemical resist using a spatially structured optical field produced by a physical photomask. Patterning can alternatively be achieved, without a mask nor structured optical fields, by methods that exploit inherent asymmetries in light-matter interactions.[4,5] These techniques can provide control of the structural evolution and morphology of a deposit by manipulation of the character of illumination (e.g. wavelength), and generate features on length scales below the optical diffraction limit despite using spatially conformal excitation.

Recently, photoelectrochemical growth of Se-Te films has been demonstrated to spontaneously yield highly ordered, periodic, anisotropic nanoscale patterns upon exposure to isotropic light fields (no photomask) produced by uncorrelated (incoherent, broadband), low-power illumination sources (mW $cm^{-2}$), with an isotropic solution in conjunction with an unpatterned, isotropic growth susbstrate.[6] In this process, illumination enhances the growth rate relative to that in the dark, by providing additional driving force for electrodeposition. Additionally, spontaneous asymmetric light scattering and absorption during growth, followed by sustained anisotropic interfacial light collection, results in highly spatially varying local growth rates that produce the observed anisotropic growth pattern in the photoelectrodeposit. The pattern anisotropy and orientation, and feature size and pitch, are correlated with the illumination polarization, and the spectral profile (wavelength distribution), respectively.[7-9] The deposit morphology is thus a physical representation of the specific photoexcitation utilized during growth, and tailoring the optical input consequently allows for the generation of complex three-dimensional (3D) nanoarchitectures.

We demonstrate herein the synthesis of PbSe nanostructures using a photoelectrochemical route analogous to that previously developed for generation of structured Se-Te deposits. In bulk and nanocrystalline forms, PbSe exhibits multiple-exciton generation upon single-photon absorption.[10,11] This phenomenon, coupled with a small electronic band gap, has enabled the generation of high-efficiency photovoltaics and high-sensitivity photodetectors with a high responsivity to mid-infrared as well as ultraviolet photons.[12-15] Addi-

tionally, PbSe is an effective thermoelectric material.[16] In this work, Se-Pb films were photoelectrodeposited with varied input polarizations and wavelengths, to evaluate the relation between the optical excitation and the resultant morphology and associated order and anisotropies. Computational modeling of the growth, involving simulations of the light-material interactions during deposition, confirmed the physics of the observed pattern development. The structured Se-Pb deposits were subsequently electrochemically processed to produce anisotropic, patterned, crystalline PbSe structures.

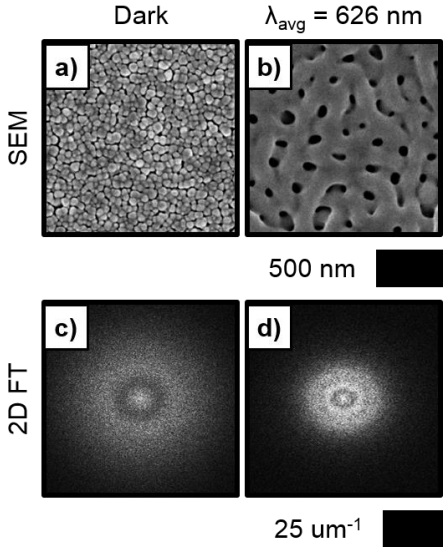


**Figure 1.** SEMs representative of deposits generated (a) in the dark and (b) using unpolarized $\lambda_{avg}$ = 626 nm illumination. (c) and (d) 2D FT generated from SEMs of the deposits depicted in (a) and (b), respectively.

The Se-Pb films were electrochemically deposited at room temperature from an aqueous solution of 0.0100 M $SeO_2$, 0.0050 M $Pb(ClO_4)_2$, and 0.100 M $HClO_4$ onto a Au-coated $n^+$-Si substrate biased for 10.00 min potentiostatically at 0.00 V versus a Ag/AgCl (3.00 M KCl) reference electrode (additional experimental details in the Supporting Information). Figure 1(a) presents a representative top-down scanning-electron micrograph (SEM) of a deposit generated in the dark, and Figure 1(b) presents a representative SEM of a deposit generated using incoherent, unpolarized illumination from a narrow-band light-emitting diode (LED) source with an intensity-weighted average wavelength, $\lambda_{avg}$, of 626 nm. The dark deposit did not exhibit substantial patterning, whereas the photoelectrodeposit displayed a mesh-type morphology that consisted of an isotropic array of nanopores that formed conformally over the entire electrode area (0.50x0.50 cm). Figure 1(c) and (d) present two-dimensional Fourier transforms (2D FTs) derived from SEM data for the dark deposit and the photoelectrodeposit, respectively. Bright regions in the 2D FT represent a periodic component in the SEM from which the 2D FT was derived. Hence the distance of a bright area from the center of the 2D FT indicates the frequency of the component, whereas the relative location indicates the direction of the periodicity. Both 2D FTs exhibited annular patterns, indicating a lack of morphological anisotropy. However, the 2D FT of the dark deposit exhibited a large annular radius with a diffuse pattern, whereas the 2D FT pattern of the photoelectrodeposit was contained within a smaller radius, and was brighter and more sharply defined. This behavior is consistent with the increased morphological homogeneity and long-range order observed in the photoelectrodeposit relative to the dark deposit (Figure 1(a) and (b)).

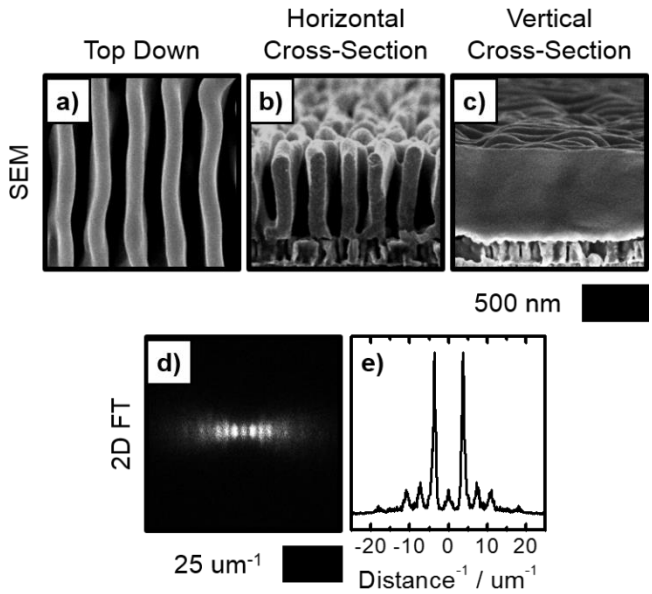


**Figure 2.** (a) Top-down SEM representative of photoelectrodeposits generated with vertically polarized $\lambda_{avg}$ = 626 nm illumination. (b) and (c) Same as (a) but cleaved along the horizontal, and vertical, axes, respectively, and acquired in cross section. (d) 2D FT generated from a top-down SEM of the deposit depicted in (a), and (e) Fourier spectrum derived from this 2D FT.

Figure 2(a) presents a representative top-down SEM of a photoelectrodeposit generated using vertically polarized $\lambda_{avg}$ = 626 nm illumination. Figure S6 presents similar data but with the use of horizontal polarization. Both SEMs reveal highly anisotropic lamellar morphologies wherein the long axes of the lamellae were oriented parallel to the polarization axis. Patterns were conformal over entire electrode areas. Figure 2(b) and (c) present analogous SEMs as in (a) that were acquired in cross-sectional view from samples that had been cleaved along the horizontal, and along the vertical, axes, respectively. The cross-sectional SEM acquired by cleaving the sample perpendicular to the polarization axis (Figure 2(b)) provides a perspective looking down the lamellar axis, and highlights the high aspect ratio of the lamellar features and thus the substantial out-of-plane anisotropy of the photoelectrodeposit. Comparison between this cross-section with that acquired by cleaving the sample parallel to the polarization axis (Figure 2(c)) demonstrates the in-plane morphological anisotropy. Figure

2(d) presents a 2D FT generated from a top-down SEM of the deposit depicted in (a). The 2D FT had a row of spots oriented perpendicular to the polarization of the illumination, confirming the anisotropic nature of the periodicity correlated with the polarization and contrasting the annular pattern observed for the 2D FT derived from SEM data acquired from the photoelectrodeposit generated using unpolarized illumination (Figure 1(d)).

Figure 2(e) presents a Fourier spectrum obtained by integrating the grayscale intensity in the 2D FT in Figure 2(d) along a narrow band through the center and along the horizontal. In the spectrum, the inverse of the lowest-frequency local maximum is equivalent to the lamellar period (distance between two identical points on two neighboring lamellae). Quantitatively, the lamellar period was 259 ± 8 nm for deposits generated using linearly polarized $\lambda_{avg}$ = 626 nm illumination. The maxima at higher frequencies were integral multiples of the lowest maximum, and thus are overtones of a single fundamental. This observation is consistent with the contrast in the SEMs (Figure 2(a) and (b)), suggesting that the topological profile is not perfectly described by a sinusoidal function. Figure 3(a) and (b) present representative SEMs of photoelectrodeposits generated using vertically polarized narrow-band LED sources with $\lambda_{avg}$ = 528 nm and 859 nm, respectively. Both photoelectrodeposits exhibited an ordered lamellar morphology in which the long axes of the lamellae were oriented vertically. However, the use of $\lambda_{avg}$ = 528 nm illumination produced smaller lamellar features, with a smaller apparent period, than was observed in photoelectrodeposits formed using $\lambda_{avg}$ = 626 nm (Figure 2(a)). Similarly, use of $\lambda_{avg}$ = 859 nm illumination resulted in the generation of larger features with a larger apparent period. Fourier analysis indicated periods of 212 ± 6 nm and 335 ± 16 nm for photoelectrodeposits generated with $\lambda_{avg}$ = 528 nm and 859 nm illumination, respectively. The control of the Se-Pb photoelectrodeposit morphology observed herein by setting $\lambda_{avg}$ and the polarization thus definitively confirms that the light-directed deposition technique is not limited to Se-Te alloys, but is a more general property of the interactions between light and matter.

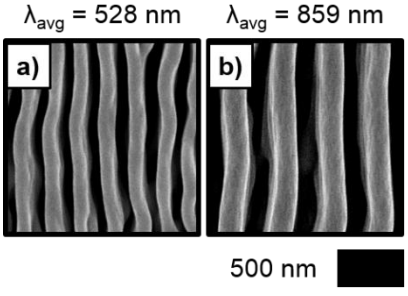


**Figure 3.** (a) and (b) SEMs representative of photoelectrodeposits generated using vertically polarized illumination with the indicated $\lambda_{avg}$.

Simulations of the growth were performed to evaluate the physics underlying the formation of the observed photoelectrodeposit nanopatterns. A two-step iterative model was utilized, wherein full-wave electromagnetic simulations were used to calculate the local photocarrier-generation rates at the growth interface (full modeling and simulation details in the Supporting Information).[6,7] Electrochemical mass addition was then simulated via a Monte Carlo method that used these generation rates to weight the local mass-addition probability. No empirical data were used in the model other than estimates of the complex index of refraction, charge-carrier concentrations, and excited-state lifetimes of the Se-Pb material. The computational results are therefore fully a consequence of the fundamental light-material interactions during growth.

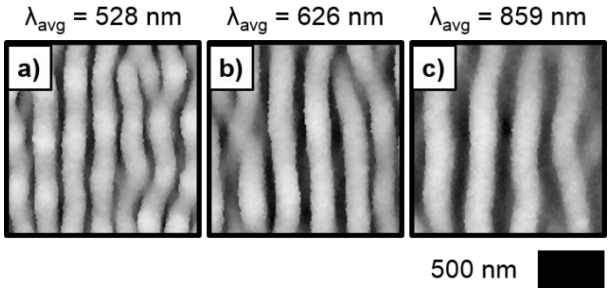


**Figure 4.** (a)-(c) Simulated photoelectrodeposit morphologies generated using vertically polarized illumination with the indicated $\lambda_{avg}$.

Figure 4 presents simulated morphologies for photoelectrodeposition using vertically polarized sources with $\lambda_{avg}$ = (a) 528 nm, (b) 626 nm and (c) 859 nm. Inspection of these simulated structures indicates excellent agreement with the observed SEM data (Figure 3(a), Figure 2(a) and Figure 3(b)). The simulations revealed a monotonic increase in lamellar period with $\lambda_{avg}$ with values of 225 ± 10 nm, 253 ± 10 nm and 321 ± 12 nm for deposition with $\lambda_{avg}$ = 528 nm, 626 nm, and 859 nm, illumination, respectively. These periods are quantitatively in accord with the actual SEM data, confirming that the nanopatterning is directed by the light-matter interactions during deposition and is principally defined by the specific illumination utilized. Additional modeling and description of these interactions is presented in the Supporting Information.

Figure 5(a) presents energy-dispersive X-ray (EDX) spectra acquired from a photoelectrodeposit generated with vertically polarized $\lambda_{avg}$ = 626 nm illumination. The solid trace corresponds to the as-deposited sample and contains Se Lα and Pb Lα signals that originated from the photoelectrodeposit, in addition to a substrate Au Lα signal. Quantification of the EDX data indicated that the as-deposited Se-Pb films had a 3 : 1 Se : Pb atomic ratio. To produce stoichiometric PbSe, after growth the photoelectrodeposits were transferred to 0.500 M $H_2SO_4$(aq) and were biased cathodically, thereby effecting reductive elimination of excess Se.[17,18] The dashed trace in Figure

5(a) presents an EDX spectrum of a photoelectrodeposit after cathodic polarization. A decrease in the intensity of Se Lα signal was observed relative to the spectrum of the as-prepared deposit, and quantification revealed a 1 : 1 Se : Pb atomic ratio. Figure 5(b) presents a representative SEM of a photoelectrodeposit generated with vertically polarized $\lambda_{avg}$ = 626 nm illumination after cathodic polarization. After removal of excess Se, an anisotropic, periodic lamellar-type pattern was observed with a nearly-identical period (255 ± 6 nm), diminished feature size, and increased surface texture, relative to the as-prepared material. Figure 5(c) presents a grazing-incidence X-ray diffraction (GIXRD) pattern acquired from a processed photoelectrodeposit similar to that depicted in Figure 5(b), and shows reflections consistent with polycrystalline PbSe. Photoelectrodeposition coupled with an electrochemical post-processing step can thus enable the template-free generation of highly anisotropic and ordered 3D PbSe nanostructures.

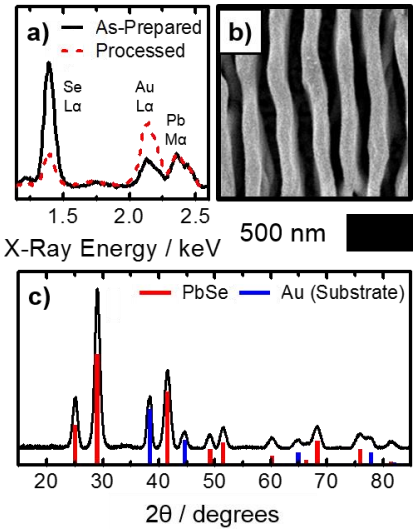


**Figure 5.** (a) EDX spectra acquired from a photoelectrodeposit generated with vertically polarized $\lambda_{avg}$ = 626 nm illumination as-prepared and after processing by cathodic polarization in 0.500 M $H_2SO_4$(aq). Representative (b) SEM and (c) GIXRD pattern of a photoelectrodeposit generated with vertically polarized $\lambda_{avg}$ = 626 nm illumination after processing by cathodic polarization in 0.500 M $H_2SO_4$(aq).

In summary, photoelectrochemical growth without structured illumination yielded spontaneous, template-free pattern formation of highly ordered, periodic Se-Pb nanostructures, with the specific deposit morphologies determined by the nature of the illumination during growth. Unpolarized illumination resulted in the generation of an isotropic mesh-type pattern, whereas linearly polarized illumination generated a highly anisotropic, lamellar-type pattern wherein the lamellar long axes were oriented parallel to the polarization axis. Lamellar feature size and period scaled proportionately with $\lambda_{avg}$. Such patterns could underpin tailored photonic structures, metamaterials, and electrocatalyst supports.[19-21] Computer modeling of the growth process based on simulations of the fundamental optical phenomena at the growth interface accurately reproduced the experimentally observed morphologies, and quantitatively matched the empirical lamellar period, confirming that the observed patterns are a consequence of the fundamental light-material interactions during growth. SEM, EDX, and GIXRD analysis collectively indicated that cathodic polarization of the Se-Pb structures in $H_2SO_4$(aq) provided a facile, general method to produce patterned nanostructures of stoichiometric, polycrystalline PbSe.

## ASSOCIATED CONTENT

**Supporting Information**.

The Supporting Information is available free of charge on the ACS Publications website.

Details regarding experimental and modeling/simulation methods, chronoamperometry data, additional scanning-electron micrographs and associated 2D FT data, additional computer simulation data, additional GIXRD data (PDF)

## AUTHOR INFORMATION

### Corresponding Author

*Email: nslewis@caltech.edu.

### Author Contributions

⊥These authors contributed equally (AIC and KRH).

## ACKNOWLEDGMENT

This work was supported by the "Light-Material Interactions in Energy Conversion" Energy Frontier Research Center funded by the U.S. Department of Energy, Office of Science, Office of Basic Energy Sciences under Award Number DE-SC0001293. The authors gratefully acknowledge R. Gerhart for assistance with photoelectrochemical cell fabrication, and M. Meier and S. Yalamanchili for assistance with computer simulations. AIC acknowledges a Graduate Research Fellowship from the National Science Foundation.

## REFERENCES

(1) Kelzenberg, M. D.; Boettcher, S. W.; Petykiewicz, J. A.; Turner-Evans, D. B.; Putnam, M. C.; Warren, E. L.; Spurgeon, J. M.; Briggs, R. M.; Lewis, N. S.; Atwater, H. A. *Nat. Mater.* **2010**, *9*, 239-244.

(2) An, S. J.; Chae, J. H.; Yi, G.-C.; Park, G. H. *Appl. Phys. Lett.* **2008**, *92*, 121108.

(3) Lin, V. S.-Y.; Motesharei, K.; Dancil, K.-P. S.; Sailor, M. J.; Ghadiri, M. R. *Science* **1997**, *278*, 840-843.

(4) Tan, C.; Qin, C.; Sadtler, B. *J. Mater. Chem. C* **2017**, *5*, 5628-5642.

(5) Dasog, M.; Carim, A. I.; Yalamanchili, S.; Atwater, H. A.; Lewis, N. S. *Nano Lett.* **2016**, *16*, 5015-5021.

(6) Sadtler, B.; Burgos, S. P.; Batara, N. A.; Beardslee, J. A.; Atwater, H. A.; Lewis, N. S. *Proc. Natl. Acad. Sci. U. S. A.* **2013**, *110*, 19707-19712.

(7) Carim, A. I.; Batara, N. A.; Premkumar, A.; Atwater, H. A.; Lewis, N. S. *ACS Nano* **2016**, *10*, 102-111.

(8) Carim, A. I.; Batara, N. A.; Premkumar, A.; May, R.; Atwater, H. A.; Lewis, N. S. *Nano Lett.* **2016**, *16*, 2963-2968.

(9) Carim, A. I.; Batara, N. A.; Premkumar, A.; Atwater, H. A.; Lewis, N. S. *Nano Lett.* **2015**, *15*, 7071-7076.

(10) Ellingson, R. J.; Beard, M. C.; Johnson, J. C.; Yu, P.; Micic, O. I.; Nozik, A. J.; Shabaev, A.; Efros, A. L. *Nano Lett.* **2005**, *5*, 865-871.

(11) Pijpers, J. J. H.; Ulbricht, R.; Tielrooij, K. J.; Osherov, A.; Golan, Y.; Delerue, C.; Allan, G.; Bonn, M. *Nat. Phys.* **2009**, *5*, 811-814.

(12) Schaller, R. D.; Klimov, V. I. *Phys. Rev. Lett.* **2004**, *92*, 186601.

(13) Sargent, E. H. *Nat. Photonics* **2009**, *3*, 325-331.

(14) Martin, J. M.; Hernández, J. L.; Adell, L.; Rodriguez, A.; López, F. *Semicond. Sci. Technol.* **1996**, *11*, 1740-1744.

(15) Sukhovatkin, V.; Hinds, S.; Brzozowski, L.; Sargent, E. H. *Science* **2009**, *324*, 1542-1544.

(16) Wang, H.; Pei, Y.; LaLonde, A. D.; Snyder, G. J. *Adv. Mater.* **2011**, *23*, 1366-1370.

(17) Lister, T. E.; Stickney, J. L. *J. Phys. Chem.* **1996**, *100*, 19568-19576.

(18) Colletti, L. P.; Flowers, B. H.; Stickney, J. L. *J. Electrochem. Soc.* **1998**, *145*, 1442-1449.

(19) Fattal, D.; Li, J.; Peng, Z.; Fiorentino, M.; Beausoleil, R. G. *Nat. Photonics* **2009**, *4*, 466-470.

(20) Kildishev, A. V.; Boltasseva, A.; Shalaev, V. M. *Science* **2013**, *339*, 1232009.

(21) Chen, Z.; Cummins, D.; Reinecke, B. N.; Clark, E.; Sunkara, M. K.; Jaramillo, T. F. *Nano Lett.* **2011**, *11*, 4168-4175.

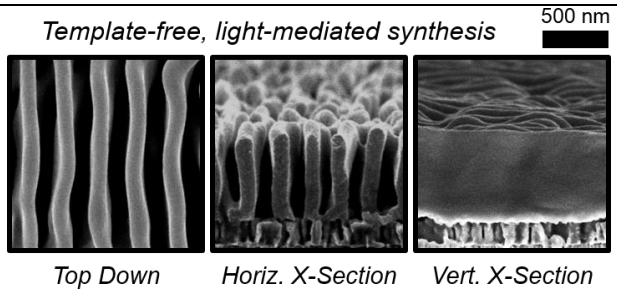
Template-free, light-mediated synthesis
500 nm
Top Down
Horiz. X-Section
Vert. X-Section